Deformation mode in 3-point flexure on pantographic block

Alessandro Ciallella, Gabriele La Valle, Antoine Vintache, Benjamin Smaniotto, François Hild

Deformation mode in 3-point flexure on pantographic block

Alessandro Ciallella*[1], Gabriele La Valle[2,1], Antoine Vintache[4], Benjamin Smaniotto[3,4], and François Hild[4]

[1]International Research Center M&MoCS, University of L'Aquila, L'Aquila, Italy

[2]Department of Engineering, University of Messina, Messina, Italy

[3]ENS Paris-Saclay, DER Génie Mécanique, Gif-sur-Yvette, France

[4]Université Paris-Saclay, CentraleSupélec, ENS Paris-Saclay, CNRS, LMPS–Laboratoire de Mécanique Paris-Saclay, Gif-sur-Yvette, France

January 23, 2023

Abstract

Pantographic blocks are metamaterials made of a finite number of parallel pantographic sheets interconnected by cylindrical pivots. In this paper, a pantographic block subjected to 3-point flexure, where the prescribed displacements are parallel to the pantographic plane, shows essentially monoclastic deformation (*i.e.,* one of the principal curvatures of the top surface is found to be negligible wrt. the other one). Pantographic blocks are modeled herein with a second gradient 3-dimensional continuum model that is valid at the length scale of a pantographic cell. This reduced order model allows for predictive numerical simulations whose computational burden is relatively small. Second gradient effects (*i.e.,* higher-order terms contributing to the strain energy) are limited to the second derivatives along the fibers of their transverse displacements. Digital Volume Correlation (DVC) techniques are employed to measure deformed shapes of pantographic blocks. A model-driven initialization procedure of DVC is followed to quantify the shape of pantographic blocks in large displacements and strains. In the present case, the previous numerical model was also used for initialization purposes.

Keywords: Digital Volume Correlation (DVC), Metamaterials, Second Gradient Continua, Pantographic block, Monoclastic Deformation.

*Corresponding Author. *alessandro.ciallella@univaq.it*

1 Introduction

In the current research efforts concerning "exotic" metamaterials and the related metamaterial synthesis problem, a special role is played by pantographic mesostructures and meso-architectures. The metamaterials synthesized by using peculiar mesostructures [TGMD17, Cia20, AYA22, BdST23] exhibit some unusual properties whose exploitation may lead to interesting engineering applications [dSA+19, dSS+19b, BDBT21, SRCC22, Spa22, ESKZ23]. Moreover, on the basis of available theoretical results [BEPd19, EAC+19, E+20, de20, SB21, ER22], when using pantographic meso-architectures as fundamental substructures at multiple length scales one may synthesize a large class of generalized continua that include at least the set of n-th gradient continua [ASd03, SAI11]. Very similar pantographic substructures may also be found in fiber-reinforced composites [CG+16, SYP+22]. It is therefore interesting to investigate the mechanical behavior of what seems to be the simplest 3D metamaterial specimen that can be assembled by using pantographic sheets [TGCR16, MLG+18, TMP+18, DASD+19, LVCF22] as elementary constituents. A first attempt to study such 3D metamaterial can be found in Refs. [ES+19, YBd20]. It was designed as a "combination" of a finite number of planar parallel pantographic sheets that are mechanically interconnected by cylindrical hinges having the same dimensions and mechanical properties as those used in each pantographic sheet (Figure 1).

A homogenized continuum model may be introduced to study the behavior of the pantographic block at the length scale of the pantographic cells. The strain energy then depends on second derivatives of the displacement field. More precisely, as they are related at the mesolevel to flexure of pantographic fibers, the second derivatives involved in the macro-strain energy are associated with transverse displacements. Pantographic blocks are therefore endowed with properties of "incomplete" second gradient continua [BdGP17, EdBS18]. For this reason, a strong anisotropy of the mechanical response of pantographic blocks is envisioned, namely, in the plane of pantographic sheets the properties correspond to those of (incomplete) second gradient materials, while in their orthogonal direction, a standard first gradient material response is expected. In this paper the expression for the deformation energy is postulated for the macro-description of pantographic blocks based on heuristic considerations taking into account the meso-architecture of the considered metamaterial, as recently introduced in [SdG+22]. The results of numerical simulations using this strain energy density have a twofold aim, namely, to initialize the DVC algorithm used to process the reconstructed volumes collected with the tomographic device available at LMPS, and to calibrate the numerical model.

Most of the materials used in mechanical and civil engineering have positive Poisson's ratios (*i.e.*, they contract laterally when stretched). However, materials characterized by negative Poisson's ratio exist and have been developed in recent years [Lak93, BSW+13]. It has to be noted that the limitations on transverse area changes due to a given elongation, summarized by the analytical statement limiting

the Poisson ratio's to the interval $[-1, 1/2]$ in isotropic and infinitesimal elasticity, are not necessarily valid in the case of second gradient and/or anisotropic materials [TC05]. The deformed shape of a medium under different loading conditions is strongly related to Poisson effects. Anticlastic, synclastic and monoclastic deformation modes are three possible observations for external surfaces [Koe84]. Anticlastic deformation corresponds to surfaces taking the shape of a saddle after flexure (*i.e.,* the two principal curvatures are opposite in sign). If the two principal curvatures have the same sign, the deformation mode is concave or convex and it is referred to as synclastic. Last, if one of the two principal curvatures is equal to zero and the other one different from zero, the deformation mode is said to be monoclastic [Pre10]. First order gradient materials generally experience anticlastic deformations when subjected to flexure [dSdSV+64, Lam91, Sea08]. The deformation mode of a pantographic block is investigated herein when loaded in three-point flexure.

In the analyses presented in this paper, Digital Volume Correlation (DVC) was used to measure displacement fields of a pantographic block subjected to 3-point flexure. DVC possibly requires tailored approaches to the problems under consideration [FCG+13, VVS+22]. A new model-driven DVC step was introduced to initialize the minimization scheme. The most interesting effects concern pantographic blocks subjected to large displacements and strain regimes. This feature required sophisticated initialization as standard algorithms may fail under these conditions dealing with periodic mesostructures and very large deformations. The outline of the paper is the following. In Section 2, the continuum second gradient model used for simulating the behavior of the pantographic block is introduced. The experimental setup is then discussed, and simulations are used to produce a proper initialization for the DVC analysis. All the preliminary steps of FE-based DVC are provided. In Section 3, the DVC results are discussed and compared with numerical simulations obtained via the proposed theoretical model (Section 4).

2 Model-Initialized DVC of In-Situ Flexure

In this section, the selected second gradient model is introduced. The experimental setup is then discussed. The simulations according to the model were used to initialize the DVC analyses.

2.1 Strain energy of pantographic blocks

The pantographic block (Figure 1) is characterized by an internal architecture organized along three distinct orthogonal directions. Two of them define the pantographic plane of the scissor mechanism whose unit vectors $\mathbf{L}$ and $\mathbf{M}$ in the reference configuration give the directions of the so-called fibers (or beams). The third direction is described by vector $\mathbf{N}$, and represents the axis of the column of the

hinges. Introducing the standard deformation tensor $\boldsymbol{F}$, namely, the gradient of the placement field, the current images of these three vectors are appraised as

$$\lambda\,\boldsymbol{l} = \boldsymbol{F}\mathbf{L}, \quad \mu\,\boldsymbol{m} = \boldsymbol{F}\mathbf{M}, \quad \eta\,\boldsymbol{n} = \boldsymbol{F}\mathbf{N} \tag{1}$$

where $\boldsymbol{l}$, $\boldsymbol{m}$, $\boldsymbol{n}$ are the unit vectors in the current (deformed) configuration under the transformation $\boldsymbol{F}$.

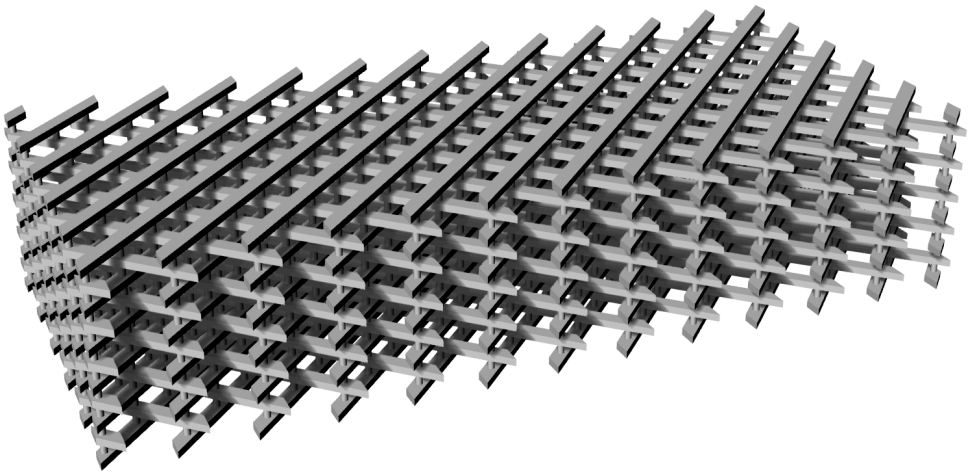

Figure 1: Nominal geometry of a pantographic block

It is assumed that the behavior of the pantographic block is the same for all planes parallel to the one on which $\mathbf{L}$ and $\mathbf{M}$ lay (*i.e.,* π), and is characterized by the strain energy [GRT17, TGGD17, Gio21]

$$\begin{aligned} w_\pi = \frac{1}{2}\,\big[&\mathrm{K}_e((\lambda-1)^2+(\mu-1)^2)+\mathrm{K}_s\gamma^2+\\ &\mathrm{K}_t\,(\kappa_{tL}^2+\kappa_{tM}^2)+\mathrm{K}_n\,(\kappa_{nL}^2+\kappa_{nM}^2)+\mathrm{K}_g\,(\kappa_{gL}^2+\kappa_{gM}^2)\big] \end{aligned} \tag{2}$$

that has two main contributions, namely, i) the first-gradient part based on the measures of deformation $(\lambda-1)$, $(\mu-1)$, and γ, which represent the change of length in the directions $\mathbf{L}$ and $\mathbf{M}$ as well as the change of angle between these two directions in the deformation process from the reference to the current configuration as defined by Equation (3); ii) the second-gradient part based on the measures of deformation representing twist and curvature in the directions $\mathbf{L}$ and $\mathbf{M}$, respectively. Specifically, the distortion angle between $\mathbf{L}$ and $\mathbf{M}$ is evaluated as

$$\sin\gamma = \boldsymbol{l}\cdot\boldsymbol{m} \tag{3}$$

while the measures of twist deformation, flexure normal to the plane π, and geodesic flexure read

$$\kappa_{tL} = (\boldsymbol{n} \times \boldsymbol{l}) \cdot \frac{\mathrm{d}\boldsymbol{n}}{\mathrm{d}S_L}, \quad \kappa_{nL} = \boldsymbol{n} \cdot \frac{\mathrm{d}\boldsymbol{l}}{\mathrm{d}S_L}, \quad \kappa_{gL} = -(\boldsymbol{n} \times \boldsymbol{l}) \cdot \frac{\mathrm{d}\boldsymbol{l}}{\mathrm{d}S_L} \tag{4}$$

and

$$\kappa_{tM} = (\boldsymbol{n} \times \boldsymbol{m}) \cdot \frac{\mathrm{d}\boldsymbol{n}}{\mathrm{d}S_M}, \quad \kappa_{nM} = \boldsymbol{n} \cdot \frac{\mathrm{d}\boldsymbol{m}}{\mathrm{d}S_M}, \quad \kappa_{gM} = -(\boldsymbol{n} \times \boldsymbol{m}) \cdot \frac{\mathrm{d}\boldsymbol{m}}{\mathrm{d}S_M} \tag{5}$$

for the fibers along the directions **L** and **M**, respectively. In Equations (4) and (5), S_L and S_M are the abscissas along the two fiber directions. The energy density (2) is based on a Kirchhoff beam model [Gio20, Gre20].

The behavior in the direction **N** was assumed to be only characterized by a first-gradient model

$$w_N = \frac{1}{2}\left\{\mathrm{K}_{eN}(\eta-1)^2 + \mathrm{K}_{sN}(\gamma_{LN}^2 + \gamma_{MN}^2) + 2\,\mathrm{K}_c\left[(\lambda-1)(\eta-1) + (\mu-1)(\eta-1)\right]\right\} \tag{6}$$

where the first contribution represents a storage of elastic energy due to a change of length in the direction **N**; the second part is related to shear in directions **L** and **N** as well as **M** and **N**; the last term represents an exchange of energy between stretching modes in the pantographic plane π and the orthogonal direction **N**. In particular, the shear strains are defined as

$$\sin\gamma_{LN} = \boldsymbol{l} \cdot \boldsymbol{n}, \quad \sin\gamma_{MN} = \boldsymbol{m} \cdot \boldsymbol{n} \tag{7}$$

where K_e, K_s, K_t, K_n, K_g, K_{eN}, K_{sN}, and K_c are material parameters. It is then assumed that the strain energy density is the sum of the two contributions given by Equations (2) and (6).

2.2 Experimental setup

The specimens under investigation were fabricated via selective laser sintering (SLS) from PA2200 polyamide powder at Warsaw University of Technology, starting from the designed nominal geometry shown in Figure 1. The pantographic block was a rectangular cuboid of sides 121.8 mm, 56.8 mm, and 26 mm, in which the pantographic sheets had dimensions 121.8×56.8 mm^2, and the length of the specimen in the direction parallel to the pivots was 26 mm. An in situ 3-point flexural test was performed by prescribing a displacement in the pantographic plane, parallel to the side whose length was 56.8 mm. These directions are referred to as longitudinal, vertical and transverse, which are associated with the $\{x\}$, $\{z\}$ and $\{y\}$ axes, respectively. The beams of the scissor pantographic mechanism belong to the planes $\{x, z\}$, while the pivots are cylinders whose axes are parallel to $\{y\}$. The designed structure had 11 layers of beams and every pair of successive layers was connected with

138 hinges (*i.e.,* 13 vertical rows of 6 hinges alternating with 12 rows of 5 hinges), for a total of 1380 hinges. The beams had a rectangular cross-section of 2×1 mm^2, and the connecting cylinders had a diameter of 0.90 mm with a length of 1.5 mm.

The 3-point flexural test was performed by prescribing a displacement in the pantographic plane, parallel to the vertical z axis. The test was monitored via micro-computed x-ray tomography [MW14] to acquire 3D scans of the reference and deformed configurations [BMA+10]. The supports were made of ABS, printed with Fused Deposition Modeling (FDM). Two supports were fixed to the bottom plate on the testing machine at a distance of 8.2 mm, and the last one to the top plate, in correspondence to the middle horizontal position of the others. The test was conducted up to the stroke limit of the testing machine, controlling the motion of the lower supports. Corrugated cardboard (*i.e.,* undulated polypropylene sheet) was placed between the specimen and the supports to prevent locking of the beam ends with respect to the supports.

Six tomographic scans were acquired during the experiment. Two scans corresponded to the unloaded configuration, the first one used as the reference scan while the second one, was used to evaluate measurement uncertainties and the baseline level for the correlation residuals. The other four scans were acquired in the deformed configurations for increasing stroke. After the acquisition of the undeformed scans, a 10-mm spacer was installed to allow for larger displacements at the stoke limit of the testing machine. The first scan was acquired after an additional 14 mm stroke. The next three scans were acquired every 5 mm, so that scans 1 to 4 were acquired for a total prescribed displacement of 24, 29, 34, and 39 mm, respectively. The hardware parameters of the experiment are reported in Table 3. The reconstructed volumes represented 143 mm$\times$40.75 mm$\times$67.48 mm with 83 µm / vx resolution corresponding to $1723 \times 491 \times 813$ voxels.

In Figure 2 a section of three of the reconstructed volumes is shown (*i.e.,* reference configuration and scans corresponding to 24 and 39 mm prescribed displacements). For the sake of conciseness, most results will focus on these last two scans. The section was initially parallel to the pantographic plane so that a fiber layer is clearly visible in the unloaded configuration (Figure 2(a)). In Figure 2(b,c), the sections were no longer parallel to the fiber layer due to out-of-plane motions. The hinges connecting the layers are visible as small white dots. The deformation of the beams was very large, especially for the last deformation level (Figure 2(c)). The magnitude of the vertical displacements was equal to hundreds of voxels, which was very challenging for DVC analyses.

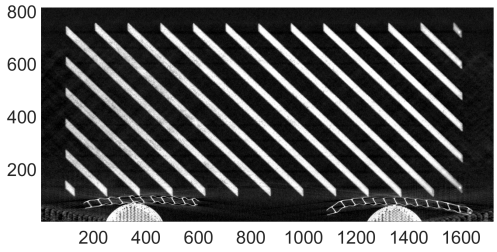

(a)

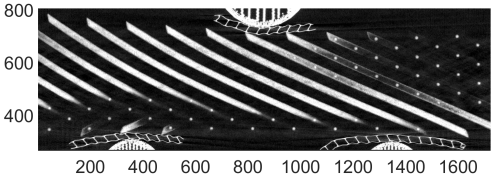

(b)

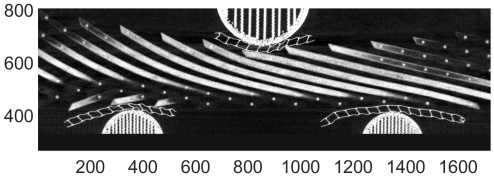

(c)

Figure 2: Sections in the pantographic plane $\{x, z\}$ for the different scanned configurations: (a) reference (unloaded) configuration; (b) 24 mm and (c) 39 mm prescribed displacements. Axis labels are expressed in voxels.

The reaction force and stroke were continuously recorded during the test (Figure 3). At zero displacement of the actuator, a large vertical black bar is shown, which shows the fluctuation of the reaction forces during the acquisition of the scans in the unloaded configuration, as well as during the installation of the spacers. From 0 to 10 mm, there were no available data. The reaction force measured during the loading steps is illustrated in light gray. The four successive vertical black bars correspond to force acquisitions during tomographic scans. The plot essentially shows a linear response. However, a small hardening effect appeared in the last part of the loading history, which was related to the triggering of fiber flexure for large displacements, and corresponded to the activation of second gradient contributions of of the placement field. In the first part of the loading history, the beams actually tended not to deform, as it is less costly in terms of energy to concentrate the deformation in the connecting hinges. It is worth noting the beams remained almost unbent up to the first deformation step (Figure 2(b)), while in the next loading steps increasing flexure of the beams occurred (Figure 2(c)). These higher order terms are not present in classical Continuum Mechanics theories. Thus, it is crucial to understand them to fully characterize this type of metamaterial [GGB17]. In the present experiment, the energy contribution associated with the elongation of the fibers was expected to be negligible [Spa20]. No significant nonlinear deformation mechanisms (*i.e.,* plasticity and/or damage) appeared during the tests as evidenced by the essentially linear response.

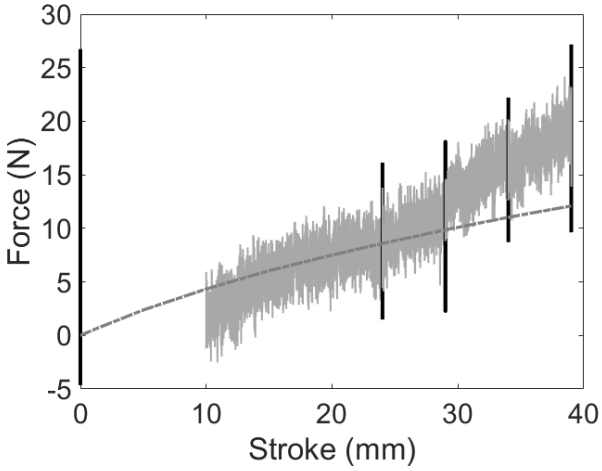

Figure 3: Comparison between measured force vs. prescribed displacement of the specimen during scan acquisition (vertical black bars) as well as loading steps (light gray), and predicted response via FE simulations (dash-dotted dark gray line).

2.3 Parameter calibration

A heuristic calibration of the model parameters was performed herein to fit the force-stroke response (Figure 3) up to the first loading step (*i.e.,* 24 mm deflection). The calibrated parameters are reported in Table 1. While the simulation proved to be robust even for larger deflections (*i.e.,* up to 39 mm), thereby allowing for the initialization of incremental DVC analyses, the force-displacement plot resulting from the simulations was less consistent for strokes beyond the second loading step (*i.e.,* 29 mm deflection, see Figure 3).

Table 1: Calibrated model parameters

K_e	1.4×10^5 N/m
K_s	13 N/m
K_g	9.5×10^{-2} Nm
K_n	1.2×10^{-2} Nm
K_t	10^{-2} Nm
K_{eN}	6.5 MN/m^2
K_{sN}	35 MN/m^2
K_c	2.6 MN/m^2

2.4 Mesh in the reference configuration

FE-based DVC [RHVB08, HBC+16] was to be utilized in the analyses of the previous test. The sought displacement field $\mathbf{u}$ is expressed as

$$\mathbf{u}(\mathbf{x}, \{\boldsymbol{v}\}) = \sum_i v_i \mathbf{N_i}(\mathbf{x}), \tag{8}$$

where $\mathbf{N_i}(\mathbf{x})$ are the vectorial shape functions associated with the nodal displacements v_i, gathered in the column vector $\{\boldsymbol{v}\}$, which are the unknowns to be measured. To determine them, the sum of squared differences are minimized over the considered region of interest (ROI), *i.e.,* given ρ the gray level residual computed for each voxel belonging to the ROI

$$\rho(\mathbf{x}, \{\boldsymbol{v}\}) = I_0(\mathbf{x}) - I_t(\mathbf{x} + \mathbf{u}(\mathbf{x}, \{\boldsymbol{v}\})), \tag{9}$$

where I_0 and I_t are the gray level for every voxel in the reference and deformed scans, the measured nodal displacements read

$$\{\boldsymbol{v}\}_{meas} = \arg\min_{\{\boldsymbol{v}\}} \Phi_c^2(\{\boldsymbol{v}\}) \tag{10}$$

with

$$\Phi_c^2(\{\boldsymbol{v}\}) = \sum_{\mathbf{x} \in ROI} \rho^2(\mathbf{x}, \{\boldsymbol{v}\}). \tag{11}$$

A penalty term was considered to perform so-called Hencky-elasticity regularization [dSS+19a]

$$\Phi_m^2(\{\boldsymbol{v}\}) = \{\boldsymbol{v}\}^\top [\mathbf{K}]^\top [\mathbf{K}] \{\boldsymbol{v}\} \ , \tag{12}$$

so that, to determine the nodal displacements via regularized DVC, the weighted sum is minimized

$$\{\boldsymbol{v}\}_{\text{meas}} = \arg\min_{\{\boldsymbol{v}\}} \left(\Phi_c^2(\{\boldsymbol{v}\}) + w_m \Phi_m^2(\{\partial \boldsymbol{v}\}) \right) \ . \tag{13}$$

where $\{\partial \boldsymbol{v}\}$ denotes the column vector of incremental displacements from one analysis to the next, and $[\mathbf{K}]$ the rectangular stiffness matrix associated with bulk and free surface nodes. The regularization weight w_m is proportional to a length, referred to as regularization length ℓ_m, raised to the power 4 [TTRMH14]. Section 2.6 will discuss the choice of the regularization length.

An FE mesh of the specimen was thus needed. The starting point was the STL model of the to-be-printed pantographic structure. Figure 4 shows the mesh in the nominal configuration generated with Gmsh [GR09]. The dimensions of the beam and hinges were significantly different, as much finer details were required to mesh them. Due to small printing errors, incorrect sample placement and possible application of preload, the reference (experimental) configuration generally does not match that of the design prepared for printing. For this reason, a backtracking procedure [ALS+21] was required to fit the mesh constructed from the nominal printing geometry to the reference scan of the unloaded configuration. The backtracked mesh was finally cropped, cutting out the last two vertical rows of pivots on both sides of the specimen, which otherwise in the configuration with the maximum deformation would end up outside the monitored volume (Figure 2). The final mesh was made of

37,759 nodes and 141,882 T4 elements whose mean size (measured as the cube root of the average elementary volume) was 6 vx.

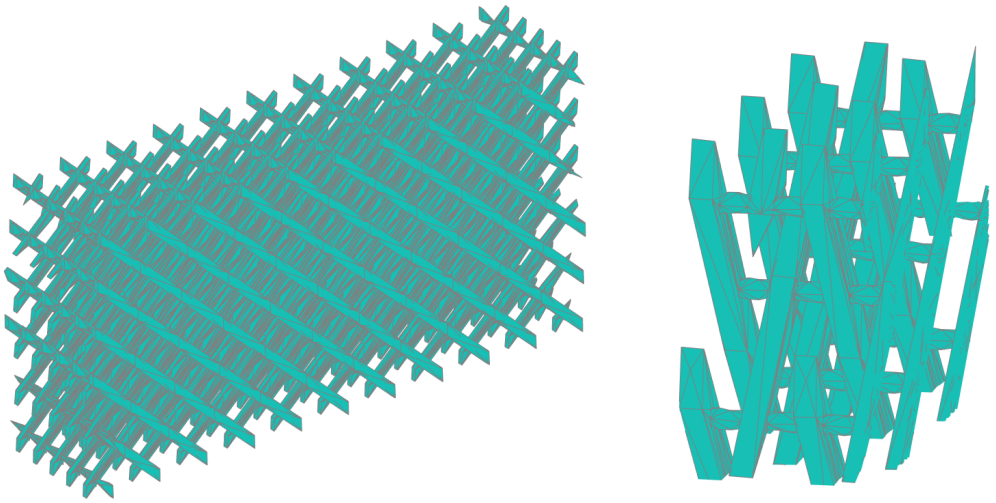

(a) (b)

Figure 4: FE mesh in the nominal configuration. Overall (a) and detail of the hinge meshing (b).

The reconstructed volumes were registered using the Correli 3.0 framework [LNM+15] in which Hencky's regularization was implemented (Table 4) since there was virtually no contrast within the printed parts. In the present case, the measured displacement field $\mathbf{u}$ was parameterized with the nodal displacements associated with the finite element discretization based on 4-noded (T4) tetrahedra [HBC+16].

2.5 DVC initialization

Large displacements between successive acquisitions of the deformed configuration (Figure 2), also due to the peculiar structure of the studied block, make it hard to deal with for DVC analyses. The latter ones had to be tailored to the present case. The prescribed displacements with respect to the reference configuration was 24, 29, 34, and 39 mm for the four deformed configurations. Expressed in voxels, they correspond to 290, 350, 410 and 470 vx. These amplitudes were therefore very large compared to the height of the specimen (*i.e.,* 56.8 mm or 684 vx). In particular, the first deformed configuration (Figure 2(b)) was the most challenging. A proper initialization of DVC analyses had then be devised to enable for convergence.

In the present case, DVC was "model-initialized," namely, finite element (FE) simulations were performed with the commercial code *COMSOL Multiphysics®* using the model introduced in Section 2.1 and calibrated in Section 2.3. A rectangular parallelepiped of size equal to that of the tested

sample size was analyzed numerically. The focus was on the material points that were located in the undeformed configuration in correspondence with the centers of mass of the pivots of the actual meta-material. The predicted positions of these material points were used to initialize the pivot motions. Elastic simulations with the backtracked mesh with prescribed pivot motions were then performed to determine the displacement of any other node.

The heuristic calibration of the material parameters for the energy density was sufficient to properly capture the overall deformation of the pantographic block. Due to buckling in the transverse direction triggered by imperfections that were not accounted for, a rigid translation only in the transverse direction had to be added as an additional correction. This phenomenon had to be accounted for due to the small dimensions of the specimens (26 mm in width), which make a displacement of the order of 5 mm (or 60 vx) observed comparable to the size of the unitary cell of the mesostructure. Figure 5 shows the positions of the hinges predicted by the numerical simulation for a 24 mm prescribed displacement drawn in one section of the first deformed volume. The prediction was quite accurate, and sufficient to ensure good initialization of the DVC algorithm.

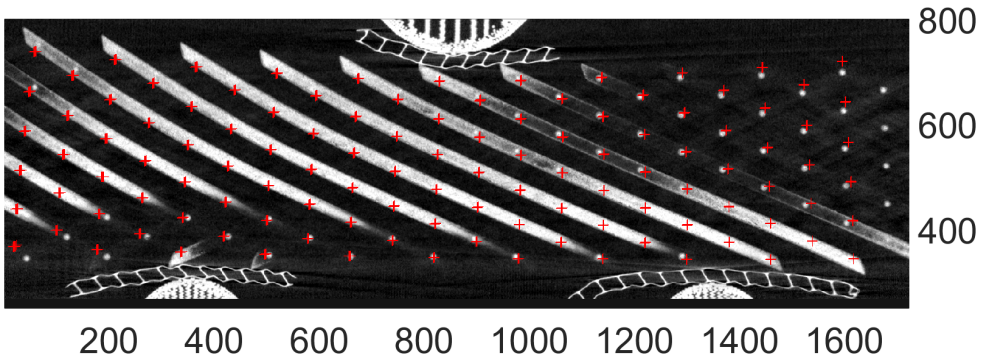

Figure 5: Numerically predicted positions of the pivots (red + symbols) drawn on a section of scan 1 (prescribed displacement 24 mm). Actual positions of the pivots are visible as small white dots. Axis labels are expressed in voxels.

2.6 Direct DVC calculations

Thanks to the previous initialization, it was then possible to run direct DVC analyses for the 4 deformed scans (*i.e.,* always using as reference the undeformed scan). The DVC calculations were stopped when the L^2-norm of displacement corrections were less than 10^{-1} vx. This level was identical to the standard displacement uncertainty (for the selected regularization length, see below) that was assessed with the repeat scan acquired prior to sample deformation.

Figure 6(a) shows the root mean square (RMS) gray level residual Φ_c versus the equilibrium gap Φ_m for different regularization lengths. The five data for each regularization length correspond, with

increasing gray level residual, to scan 0 (*i.e.,* second scan in the unloaded configuration), and then to scans 1 to 4 of the deformed configurations. The analysis of scan 0 provides information on uncertainties and on the order of magnitude of noise effects. Scans 1 to 3 have comparable residuals, suggesting that the analysis was effective for them. For the fourth scan instead, extremely high deformations resulted in higher gray level residuals. By increasing the regularization length, the equilibrium gap Φ_m decreased because more weight was given to the penalty term. It was accompanied by gray level residual increases, which remained modest up to scan 3. This observation proves that the applied regularization was consistent with the underlying material behavior. Conversely, Figure 6(b) shows that more care should be exercised for scan 4.

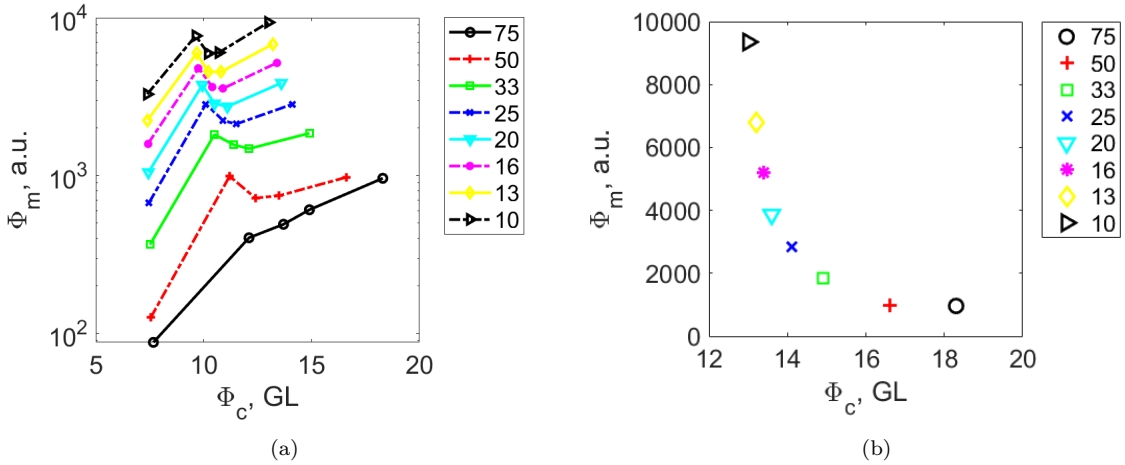

Figure 6: (a) Equilibrium gap Φ_m vs. gray level residual Φ_c for the five analyzed scans and for different regularization lengths (expressed in voxels). (b) Corresponding plot in arithmetic scale for scan 4.

One criterion used to select the optimal regularization weight is to look for the maximum curvature (*i.e.,* L-curve criterion [Han00]) in the graph above for the maximum prescribed displacement, in arithmetic scale (Figure 6(b)). According to this criterion, the regularization length $\ell_m = 25$ vx provides the best trade-off between Φ_c and Φ_m. Therefore, the regularization length $l_m = 25$ vx was selected (Table 4). For that regularization length, the gray level residuals are shown in Appendix B. Given the fact that they remained on average less than twice the level observed for the repeat scan (Figure 6(a)), the DVC analyses were deemed trustworthy.

3 DVC Results

The DVC results are discussed hereafter for the first and last deformed configurations. First, the displacement fields are analyzed. Then, the motions of the hinges are reported to assess the deformation mode of the pantographic block.

3.1 Displacement fields

The measured displacement fields in the three directions are displayed in Figures 7 and 8. As expected, the displacement amplitudes were very large compared to the overall dimensions of the specimen, and thus compared to the dimensions of the elementary pantographic cell. The flexural displacement was prescribed in the vertical direction, and the main effect was that the entire specimen shortened considerably in that direction, almost uniformly as a first approximation. The bottom of the specimen remained essentially flat, with virtually no curvature of the lower plane noticeably in correspondence with the position of the top loading support. In the upper plane, the curvature under the top support was very slight compared to the right side of the specimen and became more pronounced in the left side of the specimen (Figure 8(a), see also Figure 2). This phenomenon was due to the design of the specimen, which was chiral and in addition had an odd number of pantographic sheets. Thus one of the two beam families was predominant.

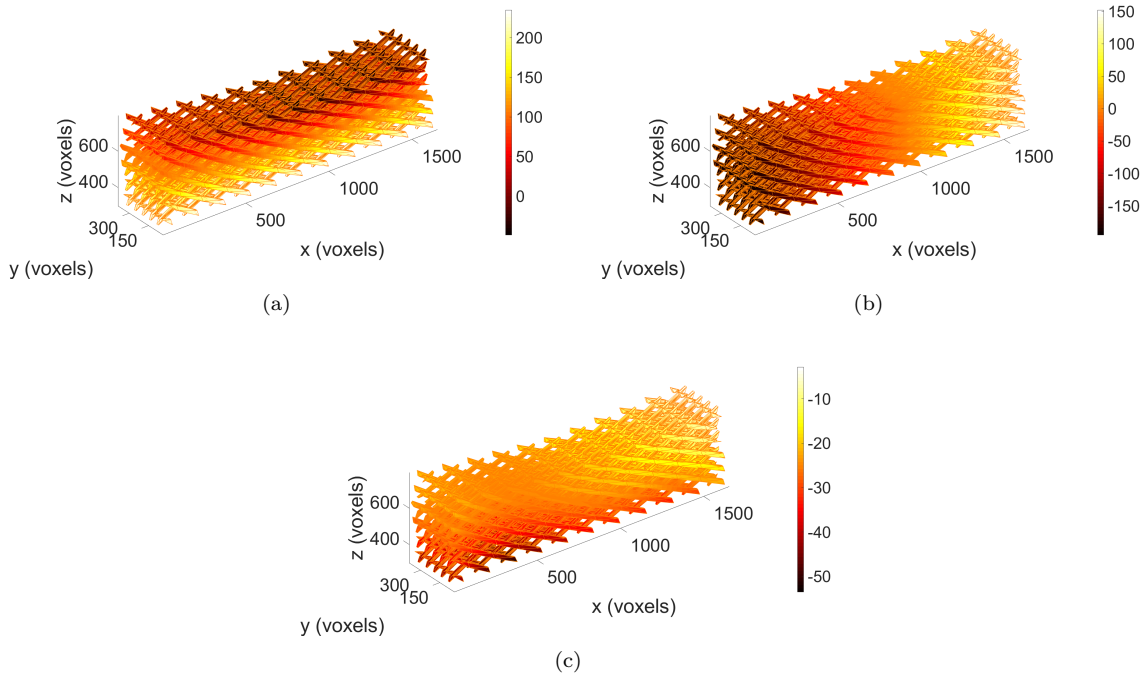

Figure 7: DVC measured vertical (a), longitudinal (b) and transverse (c) displacement fields for the first loading step (24 mm). Labels are expressed in voxels. The displacements are shown on the mesh in its deformed configuration.

The range of vertical displacement levels found for both scans was consistent with the prescribed stroke (see dynamic range of color bars in Figures 7 and 8). Specifically, the prescribed displacements of 24 and 39 mm correspond to 290 and 470 vx, respectively. It is worth noting that the minimum displacements were not equal to zero. This was due to the fact that when cropping the volumes after reconstruction, the deformed sample was centered and thus the top support had apparent translations

(Figure 2).

As a result of the mesostructure behavior, given the prescribed flexural displacement, the specimen elongated significantly in the longitudinal direction. The deformation first concentrated in the hinges, and more specifically hinge shear [CPDG22], while the beams deformed much less and the pantographic structure translated the vertical compression into longitudinal elongation. The quantification of this effect is shown in Figures 7(b) and 8(b), where longitudinal displacement measurements are shown on the deformed configurations of the specimen. The range of measured displacements was 344 vx (*i.e.,* about 28.5 mm) for the first scan and 445 vx (*i.e.,* about 36.9 mm) for the last one.

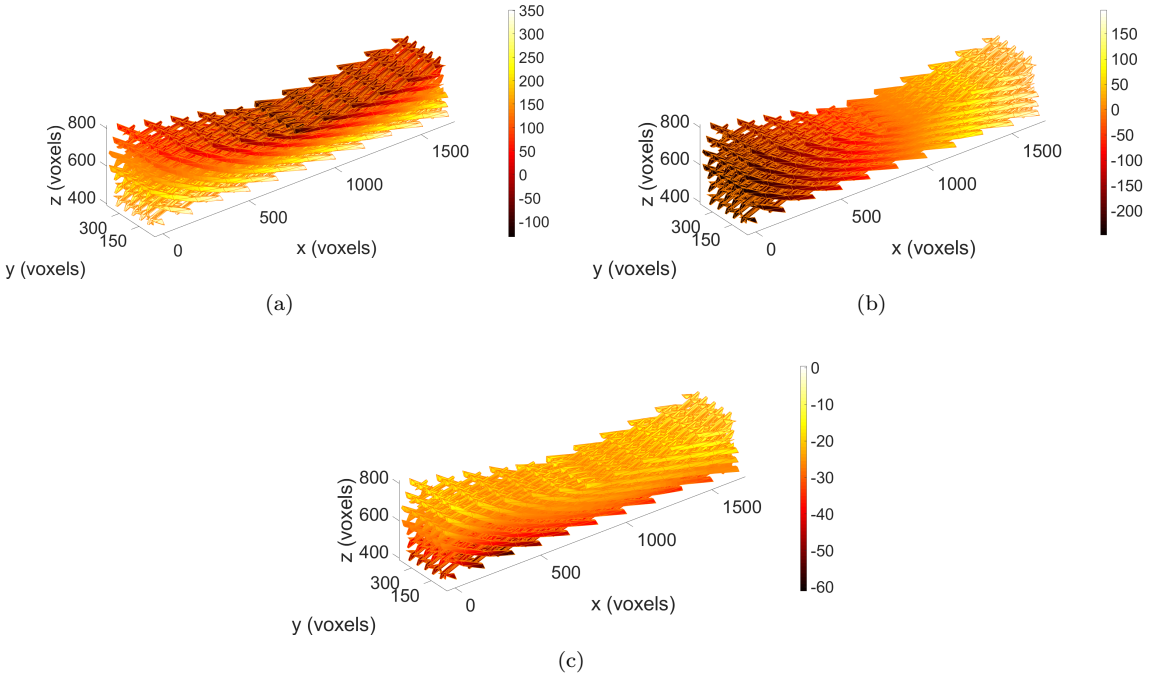

Figure 8: DVC measured vertical (a), longitudinal (b) and transverse (c) displacement fields for the last loading step (39 mm). Labels are expressed in voxels. The displacements are shown on the mesh in its deformed configuration.

Last, in the transverse direction non negligible displacements were measured with respect to the size of the elementary cell of the mesostructure. In Figures 7(c) and 8(c), the measured transverse displacements are displayed on the meshes in deformed configurations. It is interesting to note that the displacements are not significantly changing for the reported scans. The measured range varied from 52 vx for first scan 1 to 60 vx for the last one (*i.e.,* from 4.3 mm to 5 mm, respectively). This level had the same order of magnitude as the size of elementary cells in the periodic design, which was exactly 5 mm. The transverse displacements appear to be related to specimen sliding on the lower supports, particularly the left one, probably originating from printing defects that initiated buckling, and possibly imperfect specimen placement after the installation.

3.2 Hinge kinematics

From these experimental data, it is of interest to extract some information about the hinges, in particular, because the continuous model for which the energy described in Section 2.1 was postulated was built to predict the location of the geometric centers of the interconnecting hinges. Piola's identification conjecture underlies the use of the continuous model for similar mesostructured media, and the geometric centers of the hinges are chosen as control points [DAP15, dGPR16]. It was already reported how the numerical prediction of the position of the hinges in the deformed configurations was the basis of the initialization of the DVC procedure (Figure 5). Let us now address some considerations based on the analysis of the hinge motions.

Having successfully carried out FE-based DVC analyses, the behavior of various constituents of the metamaterial can be studied for different deformed configurations. The mesh elements that in the nominal geometry make up the hinges were selected. As an example, Figure 9 shows the configuration of the hinges in their reference state and in the deformed configuration with maximum deflection. One can then look for more specific information about the hinges, such as specific sections in the specimen or follow the positions of their centers of mass.

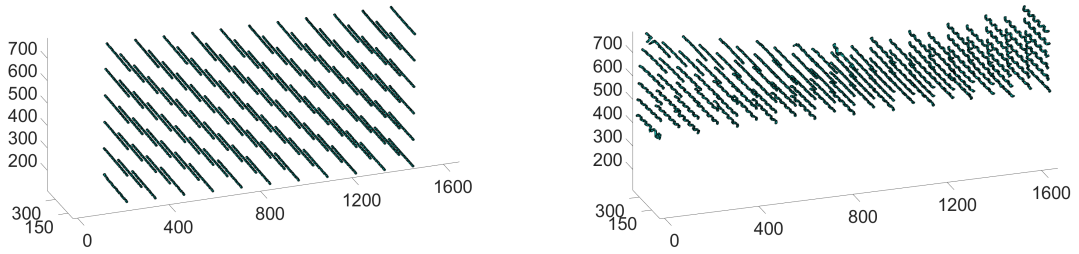

Figure 9: Configuration of hinges in the (a) reference (*i.e.,* unloaded) and (b) last deformed (*i.e.,* 39 mm deflection) configurations. Labels are expressed in voxels.

Details of Figure 9 are shown in Figure 10 where a set of hinges in the $\{y, z\}$ plane (*i.e.,* orthogonal to the pantographic plane) is plotted in the previous configurations. The cross-sections of the pantographic block remained nearly planar and rectangular. While the vertical length of the sections (parallel to the prescribed displacement) was reduced, the sides in the transverse direction (*i.e.,* orthogonal to the flexural displacement) remained almost unchanged.

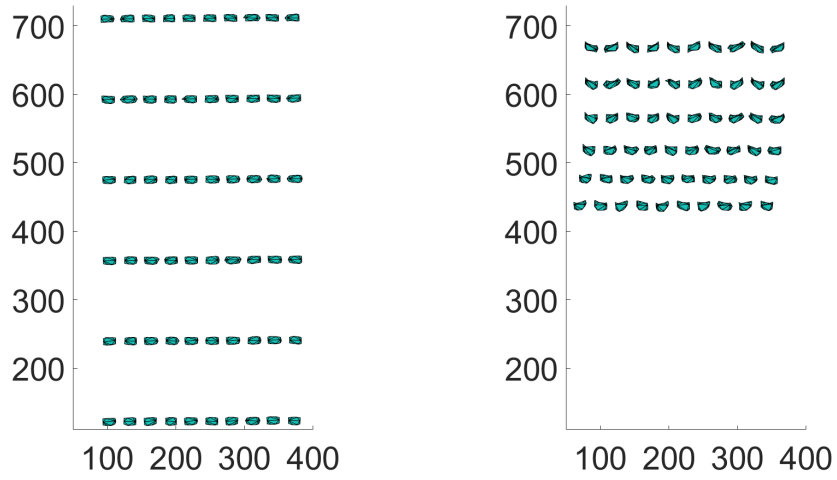

(a) (b)

Figure 10: Detail of Figure 9. Comparison of the same cross-section in the {y,z} plan for (a) the reference (*i.e.,* unloaded) and (b) last deformed (*i.e.,* 39 mm deflection) configurations. Labels are expressed in voxels.

3.3 Deformation mode

Let us now study the deformed shape of the pantographic block during the test; in particular, on the deformed shape of the top surface, which underwent maximum curvature, and analyze the type of deformation mode. The deformed surface to be studied was built by interpolating the positions of the center of mass of four consecutive central top and horizontal rows of pivots, selecting from the vertical columns with five pivots as highlighted on one $\{x, z\}$ section in Figure 11(a). This choice was made to locally study the surface of the pantographic block affected by the highest longitudinal curvature but avoiding to deal with the top pivots where artifacts may occur due to direct contact with the support.

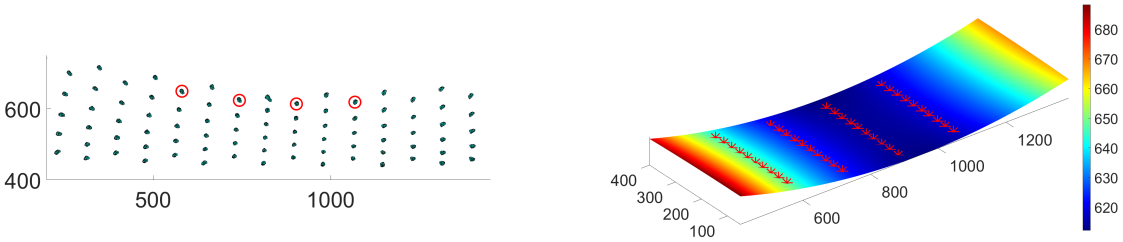

Figure 11: (a) Selected pivots for building the interpolating top surface on one {x,z} section. (b) Paraboloid interpolating the vertical positions of the center of mass of the selected pivots, and actual positions of the centers of mass of the pivots measured via DVC for 39 mm deflection (red markers). Labels are expressed in voxels.

The interpolation was performed by looking for the six coefficients of a complete second-order

polynomial interpolation $z = P_2(x, y)$ that gives the best fit of the positions of the pivots according to the least squares error. The interpolating paraboloid is then studied to evaluate the principal curvatures. In Figure 11(b), both interpolating paraboloid and actual positions of the centers of mass of the pivots measured via DVC are shown for the maximum deflection.

The curvatures of the paraboloid were investigated to distinguish the kind of deformation mode, namely, anticlastic (saddle shape), synclastic (eggshell shape) or monoclastic (cylindrical shape). The Gaussian curvature and the two principal curvatures were evaluated locally at the critical point X_C having horizontal tangent plane. Let $K(X_C) = \kappa_1(X_c)\kappa_2(X_C)$ be the Gaussian curvature, where κ_1 and κ_2 are the principal curvatures [Pre10]. The deformation mode corresponds to $K > 0$ for synclastic surfaces, $K < 0$ for anticlastic surfaces, and $K = 0$ with κ_1 and κ_2 both not vanishing for monoclastic surfaces. In the present case, the critical point was not exactly centered in the middle of the specimen but slightly shifted toward the right end, due to asymmetry of the deformed shape of the specimen already discussed. Small negative Gaussian curvatures K were found (Table 2). The principal directions associated with the principal curvatures were parallel to the longitudinal and transverse directions of the beam (as expected). The principal curvatures were both quite small, with the curvature corresponding to the transverse direction about 20% of the longitudinal one, but with opposite sign, denoting strictly speaking a weak anticlastic mode. The transverse curvature, however, was presumably increased because of out-of-plane transverse displacements of the specimen due to sliding on the supports. In addition, the transverse radius of curvature was still significantly large compared to the dimensions of the specimen sides. Overall, these observations and the smallness of the Gaussian curvature confirmed that the deformation mode was that of an essentially monoclastic surface (*i.e.,* that the deformed surface was well approximated by a monoclastic mode).

Table 2: Curvatures assessed from experimental measurements and numerical simulations

Surface	Longitudinal curvature	Transverse curvature	Gaussian curvature K
Figure 11(b)	$6.5 \times 10^{-3}\ mm^{-1}$	$-1.3 \times 10^{-3}\ mm^{-1}$	$-8.45 \times 10^{-6}\ \text{mm}^{-2}$
Figure 14	$3.8 \times 10^{-3}\ \text{mm}^{-1}$	$-8.1 \times 10^{-5}\ \text{mm}^{-1}$	$-3.08 \times 10^{-7}\ \text{mm}^{-2}$
Figure 16(a)	$12.7 \times 10^{-3}\ \text{mm}^{-1}$	$-4.6 \times 10^{-3}\ \text{mm}^{-1}$	$-5.84 \times 10^{-5}\ \text{mm}^{-2}$
Figure 16(b)	$9.9 \times 10^{-3}\ \text{mm}^{-1}$	$-4.9 \times 10^{-3}\ \text{mm}^{-1}$	$-4.81 \times 10^{-5}\ \text{mm}^{-2}$

4 Numerical Simulations

This section deals with the numerical simulations of the flexural test with the calibrated constitutive law. The predicted deformation mode is compared with actual observations. Last, another flexural configuration is proposed to induce anticlastic deformation.

4.1 Predicted deformation mode

The continuum macro-model whose energy density was postulated in Section 2.1 was further probed to predict the deformed shapes of the pantographic block in 3-point flexure. It is worth noting that the DVC analyses needed the prediction obtained by the second gradient model for the initialization step, but the final results were independent of the theoretical model. In Figures 12 and 13, the displacement fields are reported along the three directions for prescribed deflections of 24 and 39 mm, respectively, which correspond to the first and last scan of the test (Section 2.2). Similar conclusions were drawn from intermediate steps, and are thus not reported for the sake of brevity. The correspondence with the reported experimental results was very good (Figures 7 and 8). As discussed above, the only unpredicted effect was related to sliding that led to transverse displacements in the actual test. In the numerical simulations, the displacements in the transverse direction were essentially vanishing and no action triggering possible buckling was considered. Note that in all plots the lines on the model are material lines drawn to allow for easier comparison of the numerical results with the experiment and eliminate any ambiguity as to which setup was considered for the 3-point flexural test.

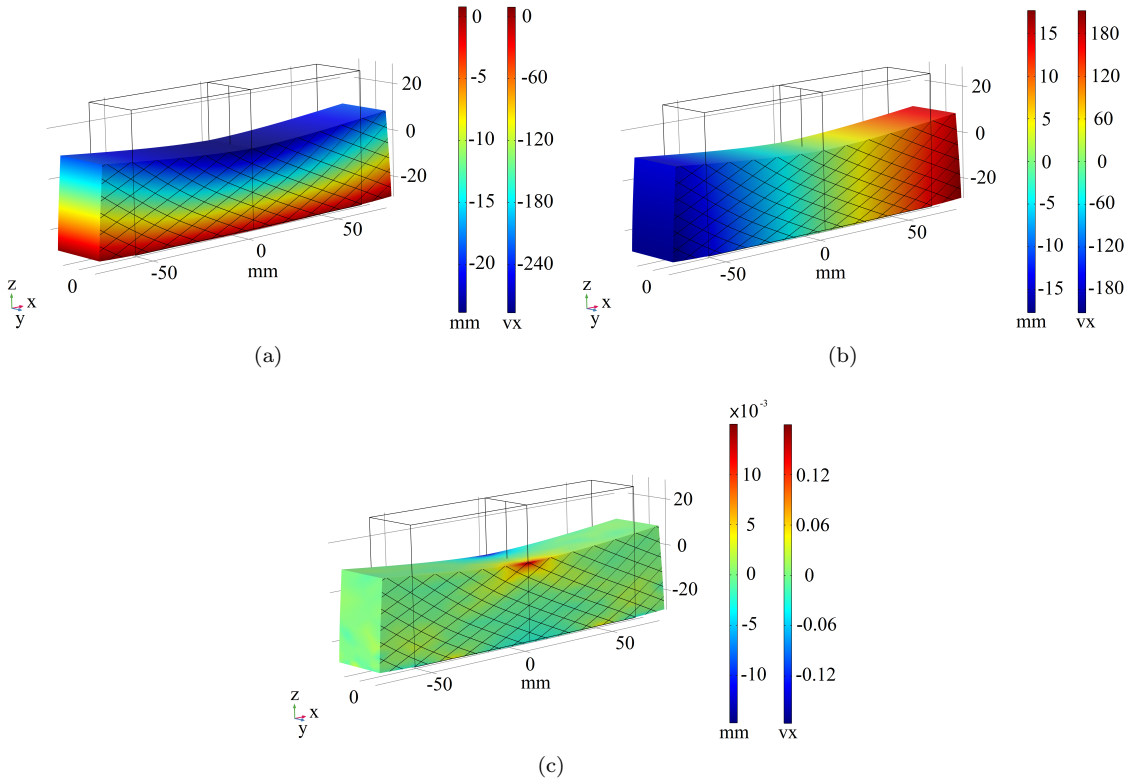

Figure 12: FE results for a prescribed deflection of 24 mm in the vertical direction. (a) Vertical, (b) longitudinal, and (c) transverse displacement fields.

The other apparent difference with the experiment concerns the range of longitudinal amplitudes.

The amplitude range was over 30 mm in Figure 12(b) and over 40 mm for Figure 13(b). As shown in Figure 5, the correspondence with the experiment was actually very good, and this apparent difference was due to the fact that the region over which the DVC analysis was performed was cropped as explained at the end of Section 2.4. Instead, the simulations were performed on a model of same size as the physical specimen for consistency with the experiment. Last, the simulations could not predict any asymmetry in terms of vertical displacements.

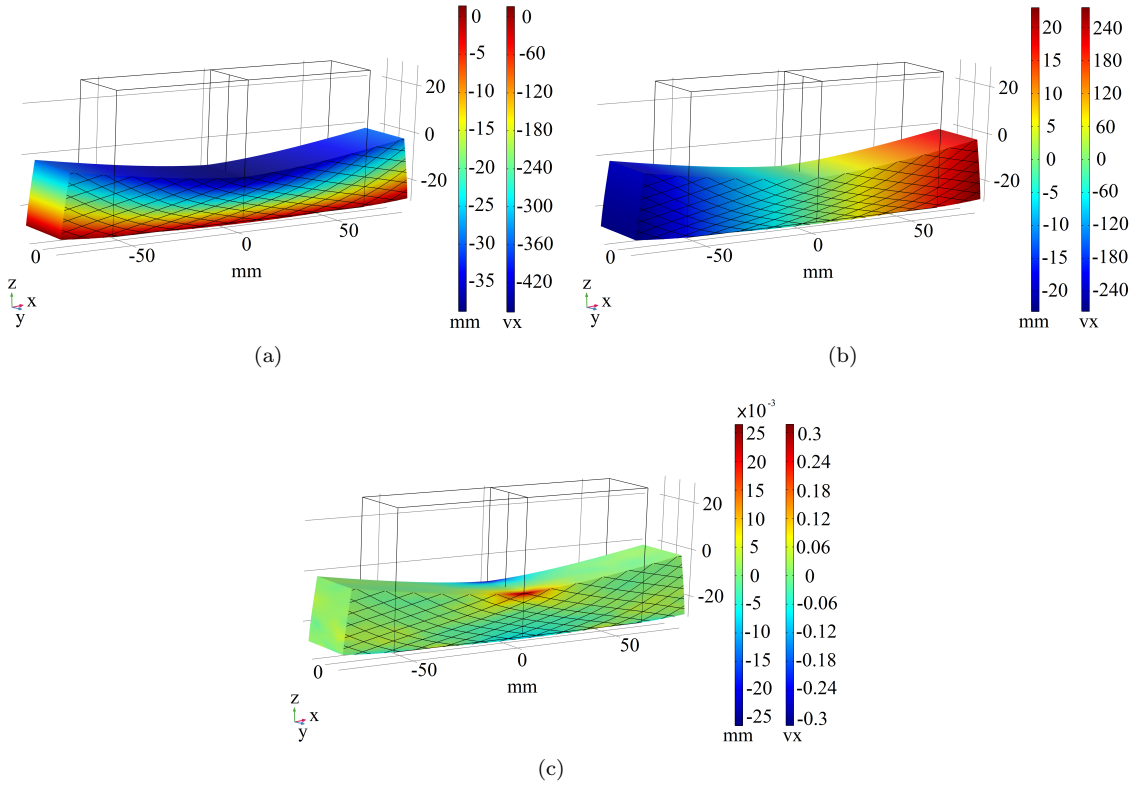

Figure 13: FE simulation results for a prescribed displacement of 39 mm in the vertical direction. (a) Vertical, (b) longitudinal, and (c) transverse displacement fields.

For the purpose of comparison with the interpolated top surface of the real experiment, the predicted deformation of the top surface was studied in the same way as before. The positions of the same pivots were interpolated with a second order polynomial, and the best fit paraboloid shown in Figure 14 was obtained. Consistent with the experiment, in the present case the Gaussian curvature K at the critical point was negligible, and the deformation mode was monoclastic. As to the longitudinal principal curvatures, the theoretical prediction is about 60% of the experimental one. In the transverse direction, the curvature was in this case very small as a consequence of the quasi-absence of strains in that direction.

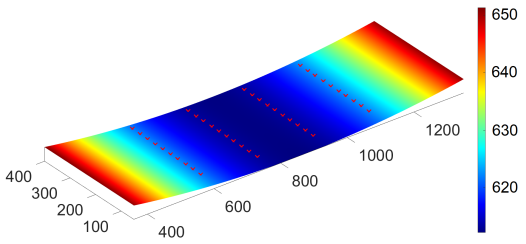

Figure 14: Paraboloid interpolating the vertical positions of the center of mass of the selected pivots, and positions of the centers of mass of the pivots predicted by numerical simulations (red markers).

4.2 Anticlastic deformation mode

Numerical simulations were finally performed for a second case in which the prescribed load was orthogonal to the pantographic plane. Investigating the behavior of such metamaterial for different loading directions is of interest given the anisotropy of the model and material. The parameters used in this new simulation were the same as those gathered in Table 1 as well as the way the boundary conditions were implemented. The FE analysis produced displacement fields shown in Figure 15; the three components of the displacement field are displayed on the deformed configuration for an applied deflection of 10 mm. A different response is observed under these new loading conditions. The bottom side of the specimen this time no longer remained flat but lowered in the middle, and raises at the ends, rotating the cross-sections. Further, the displacements in the transverse direction, *i.e.*, $\{z\}$-axis direction in Figure 15, are no longer negligible. The elongation and flexure of the pantographic planes are clearly visible.

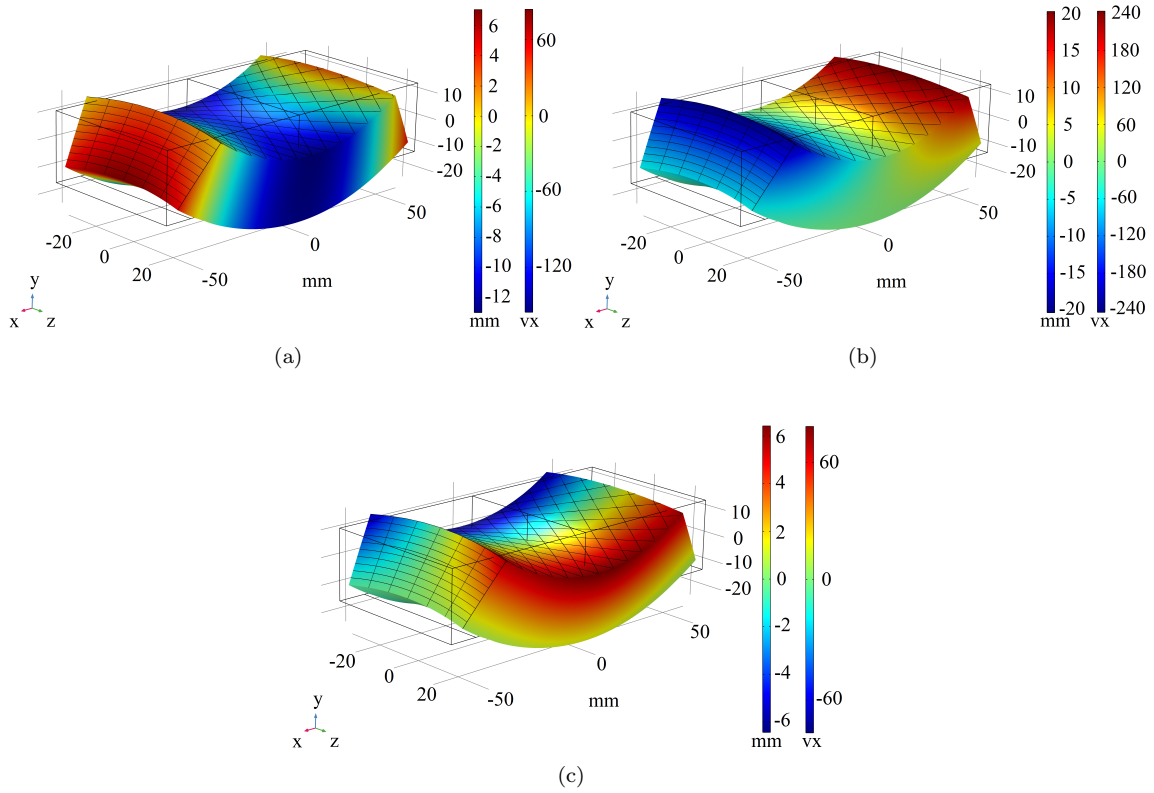

Figure 15: FE simulation results for a prescribed displacement of 10 mm in the vertical direction. (a) Vertical, (b) longitudinal, and (c) transverse displacement fields.

An anticlastic deformation mode appeared in this case, namely, the curvatures in the longitudinal and transverse directions were nonzero and of opposite sign. The top and bottom pantographic surfaces were studied constructing the paraboloid interpolation of the position of the corresponding pivots, similarly to what was previously performed in the other two cases. The top and bottom surfaces are reported in Figure 16. The Gaussian curvature was evaluated at the critical point, which is the middle point of the suface, and was found to be negative. The two principal directions associated with the principal curvatures were again the longitudinal and transverse directions. Regarding the principal curvatures, the transverse one was very close for both top and bottom surfaces, while the longitudinal one, instead, increased almost 30% from the bottom to the top surface (Table 2).

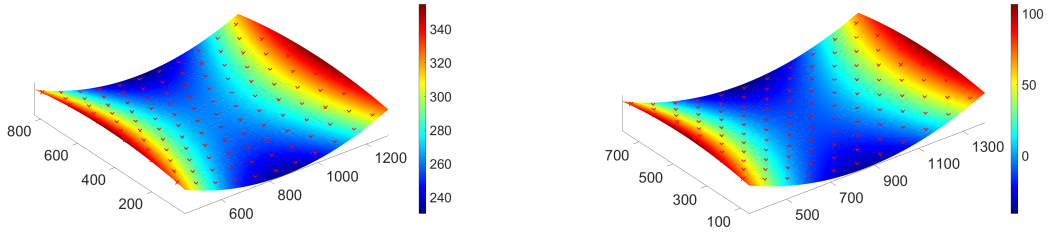

(a) (b)

Figure 16: Paraboloid interpolating the vertical positions of the center of mass of the pivots in the top (a) and bottom (b) planes, and positions of the centers of mass of these pivots predicted by numerical simulations (red markers).

5 Conclusion

For isotropic and linear elastic materials subjected to 3-point flexure, anticlastic curvatures are induced by the coupling between local transverse elongation and flexure. The latter is well described by the Saint-Venant solution [dSdSV+64, Lam91, Sea08]. Conversely, second gradient materials are governed by more general strain energies. There are material directions along which large deformations are possibly associated with very low energies. Consequently, it was envisioned that some exotic effects may arise. In this paper, it was proven via DVC analyses that a pantographic block, when subjected to 3-point flexure in which the prescribed displacements were parallel to the pantographic plane, experienced deformations well approximated by a monoclastic mode for the top surface, while it remained essentially flat at the bottom.

The second order reduced constitutive model introduced herein showed a rather satisfactory agreement with the experimental evidence, in particular in predicting the displacements and a monoclastic deformation mode. The model parameters were only calibrated at the global level (*i.e.,* based on the overall force vs. stroke curve). In the future, it is desirable to calibrate the parameters by using more kinematic data. The expected results would generalize those already reported [Fed15, Gio16, PAG17, GHD+18].

Having studied the flexural response of a pantographic block with prescribed displacements in the pantographic plane, it was natural to investigate its deformation mode when the displacements were applied in the direction orthogonal to the pantographic plane. An anticlastic mode was predicted. This difference is not surprising since the pantographic block was described by second derivatives of displacements along the pantographic planes and first derivatives along the thickness. Additional experiments are thus needed to further confirm these predictions. Other experimental campaigns are scheduled to fully validate the proposed model on tests other than 3-point flexure and to investigate the dynamic behavior of such metamaterials (see, for instance, Refs. [CGE+22, Eug22]).

The model-driven initialization for the DVC analyses proved to be very effective in overcoming the challenges due to large displacements and periodicity of the pantographic mesostructure. This procedure may also be followed when initialization is made complicated by other phenomena, such as the onset of damage or fracture, for instance using finer models [EYPT22, PTM+22].

Acknowledgment

This work has been financially supported by the French "Agence Nationale de la Recherche" through the "Investissements d'avenir" program (ANR-10-EQPX-37 MATMECA Grant) and by CNRS/IRP Coss&Vita between Fédération Francilienne de Mécanique (F2M, CNRS FR2609) and M&MoCS. The pantographic metamaterial was kindly provided by Prof. Tomasz Lekszycki and Dr. Rafal Drobnicki. This paper is dedicated to Prof. Lekszycki who passed away very recently. AC also thanks the GNFM of INDAM.

References

[ALS+21] Patrick Auger, Thomas Lavigne, Benjamin Smaniotto, Mario Spagnuolo, Francesco dell'Isola, and François Hild. Poynting Effects in Pantographic Metamaterial Captured via Multiscale DVC. *Journal of Strain Analysis for Engineering Design*, 2021.

[ASd03] Jean-Jacques Alibert, Pierre Seppecher, and Francesco dell'Isola. Truss modular beams with deformation energy depending on higher displacement gradients. *Mathematics and Mechanics of Solids*, 8(1):51–73, 2003.

[AYA22] Gokhan Aydin, M Erden Yildizdag, and Bilen Emek Abali. Strain-gradient modeling and computation of 3-d printed metamaterials for verifying constitutive parameters determined by asymptotic homogenization. In *Theoretical Analyses, Computations, and Experiments of Multiscale Materials*, pages 343–357. Springer, 2022.

[BDBT21] Emilio Barchiesi, Francesco Dell'Isola, Alberto M Bersani, and Emilio Turco. Equilibria determination of elastic articulated duoskelion beams in 2d via a riks-type algorithm. *International Journal of Non-Linear Mechanics*, 128:103628, 2021.

[BdGP17] Claude Boutin, Francesco dell'Isola, Ivan Giorgio, and Luca Placidi. Linear pantographic sheets: asymptotic micro-macro models identification. *Mathematics and Mechanics of Complex Systems*, 5(2):127–162, 2017.

[BdST23] Emilio Barchiesi, Francesco dell'Isola, Pierre Seppecher, and Emilio Turco. A beam model for duoskelion structures derived by asymptotic homogenization and its application to axial loading problems. *European Journal of Mechanics-A/Solids*, 98:104848, 2023.

[BEPd19] Emilio Barchiesi, Simon R Eugster, Luca Placidi, and Francesco dell'Isola. Pantographic beam: A complete second gradient 1d-continuum in plane. *Zeitschrift für angewandte Mathematik und Physik*, 70(5):1–24, 2019.

[BMA+10] J.Y. Buffière, E. Maire, J. Adrien, J.P. Masse, and E. Boller. In Situ Experiments with X ray Tomography: an Attractive Tool for Experimental Mechanics. *Experimental Mechanics*, 50(3):289–305, 2010.

[BSW+13] Sahab Babaee, Jongmin Shim, James C Weaver, Elizabeth R Chen, Nikita Patel, and Katia Bertoldi. 3d soft metamaterials with negative poisson's ratio. *Advanced Materials*, 25(36):5044–5049, 2013.

[CG+16] M Cuomo, L Greco, et al. Simplified analysis of a generalized bias test for fabrics with two families of inextensible fibres. *Zeitschrift für angewandte Mathematik und Physik*, 67(3):1–23, 2016.

[CGE+22] Alessandro Ciallella, Ivan Giorgio, Simon R Eugster, Nicola L Rizzi, and Francesco dell'Isola. Generalized beam model for the analysis of wave propagation with a symmetric pattern of deformation in planar pantographic sheets. *Wave Motion*, 113:102986, 2022.

[Cia20] Alessandro Ciallella. Research perspective on multiphysics and multiscale materials: a paradigmatic case. *Continuum Mechanics and Thermodynamics*, 32(3):527–539, 2020.

[CPDG22] Alessandro Ciallella, Davide Pasquali, Francesco D'Annibale, and Ivan Giorgio. Shear rupture mechanism and dissipation phenomena in bias-extension test of pantographic sheets: Numerical modeling and experiments. *Mathematics and Mechanics of Solids*, page 10812865221103573, 2022.

[DAP15] Francesco Dell'Isola, Ugo Andreaus, and Luca Placidi. At the origins and in the vanguard of peridynamics, non-local and higher-gradient continuum mechanics: an underestimated and still topical contribution of gabrio piola. *Mathematics and Mechanics of Solids*, 20(8):887–928, 2015.

[DASD+19] Michele De Angelo, Mario Spagnuolo, Francesco D'annibale, Aron Pfaff, Klaus Hoschke, Aviral Misra, Corinne Dupuy, Patrice Peyre, Justin Dirrenberger, and Marek Paw-

likowski. The macroscopic behavior of pantographic sheets depends mainly on their microstructure: experimental evidence and qualitative analysis of damage in metallic specimens. *Continuum Mechanics and Thermodynamics*, 31(4):1181–1203, 2019.

[de20] Francesco dell'Isola and David J. Steigmann eds. *Discrete and continuum models for complex metamaterials*. Cambridge University Press, 2020.

[dGPR16] Francesco dell'Isola, Ivan Giorgio, Marek Pawlikowski, and Nicola Luigi Rizzi. Large deformations of planar extensible beams and pantographic lattices: heuristic homogenization, experimental and numerical examples of equilibrium. *Proceedings of the Royal Society A: Mathematical, Physical and Engineering Sciences*, 472(2185):20150790, 2016.

[dSA+19] Francesco dell'Isola, Pierre Seppecher, Jean Jacques Alibert, et al. Pantographic metamaterials: an example of mathematically driven design and of its technological challenges. *Continuum Mechanics and Thermodynamics*, 31(4):851–884, 2019.

[dSdSV+64] Adhémar Jean Claude Barré de Saint, M de Saint-Venant, et al. *Résumé des leçons données à École des ponts et chaussées sur l'application de la mécanique à l'établissement des constructions et des machines*, volume 1. Dunod, 1864.

[dSS+19a] F. dell'Isola, P. Seppecher, M. Spagnuolo, E. Barchiesi, F. Hild, T. Lekszycki, I. Giorgio, L. Placidi, U. Andreaus, M. Cuomo, S.R. Eugster, A. Pfaff, K. Hoschke, R. Langkemper, E. Turco, R. Sarikaya, A. Misra, M. De Angelo, F. D'Annibale, A. Bouterf, X. Pinelli, A. Misra, B. Desmorat, M. Pawlikowski, C. Dupuy, D. Scerrato, P. Peyre, M. Laudato, L. Manzari, P. Göransson, C. Hesch, S. Hesch, P. Franciosi, J. Dirrenberger, F. Maurin, Z. Vangelatos, C. Grigoropoulos, V. Melissinaki, M. Farsari, W. Muller, E. Abali, C. Liebold, G. Ganzosch, P. Harrison, R. Drobnicki, L.A. Igumnov, F. Alzahrani, and T. Hayat. Advances in Pantographic Structures: Design, Manufacturing, Models, Experiments and Image Analyses. *Continuum Mechanics and Thermodynamics*, 31(4):1231–1282, 2019.

[dSS+19b] Francesco dell'Isola, Pierre Seppecher, Mario Spagnuolo, et al. Advances in pantographic structures: design, manufacturing, models, experiments and image analyses. *Continuum Mechanics and Thermodynamics*, 31(4):1231–1282, 2019.

[E+20] VA Eremeyev et al. Weak solutions within the gradient-incomplete strain-gradient elasticity. *Lobachevskii Journal of Mathematics*, 41(10):1992–1998, 2020.

[EAC+19] Victor A Eremeyev, Faris Saeed Alzahrani, Antonio Cazzani, Tasawar Hayat, Emilio Turco, Violetta Konopińska-Zmysłowska, et al. On existence and uniqueness of weak

solutions for linear pantographic beam lattices models. *Continuum Mechanics and Thermodynamics*, 31(6):1843–1861, 2019.

[EdBS18] Victor A Eremeyev, Francesco dell'Isola, Claude Boutin, and David Steigmann. Linear pantographic sheets: existence and uniqueness of weak solutions. *Journal of Elasticity*, 132(2):175–196, 2018.

[ER22] Victor A Eremeyev and Emanuele Reccia. Nonlinear strain gradient and micromorphic one-dimensional elastic continua: Comparison through strong ellipticity conditions. *Mechanics Research Communications*, page 103909, 2022.

[ES+19] Simon Eugster, David Steigmann, et al. Continuum theory for mechanical metamaterials with a cubic lattice substructure. *Mathematics and Mechanics of Complex Systems*, 7(1):75–98, 2019.

[ESKZ23] Victor A Eremeyev, Daria Scerrato, and Violetta Konopińska-Zmysłowska. Ellipticity in couple-stress elasticity. *Zeitschrift für angewandte Mathematik und Physik*, 74(1):1–9, 2023.

[Eug22] Simon Raphael Eugster. Numerical analysis of nonlinear wave propagation in a pantographic sheet. *Mathematics and Mechanics of Complex Systems*, 9(3):293–310, 2022.

[EYPT22] M Erden Yildizdag, Luca Placidi, and Emilio Turco. Modeling and numerical investigation of damage behavior in pantographic layers using a hemivariational formulation adapted for a hencky-type discrete model. *Continuum Mechanics and Thermodynamics*, pages 1–14, 2022.

[FCG+13] R. Fedele, A. Ciani, L. Galantucci, , M. Bettuzzi, and L. Andena. A regularized, pyramidal multi-grid approach to global 3d-volume digital image correlation based on x-ray micro-tomography. *Fundam. Inf.*, 125(3-4):361–376, 2013.

[Fed15] R Fedele. Simultaneous assessment of mechanical properties and boundary conditions based on Digital Image Correlation. *Exp. Mech.*, 55:139–153, 2015.

[GGB17] Leopoldo Greco, Ivan Giorgio, and Antonio Battista. In plane shear and bending for first gradient inextensible pantographic sheets: numerical study of deformed shapes and global constraint reactions. *Mathematics and Mechanics of Solids*, 22(10):1950–1975, 2017.

[GHD+18] I Giorgio, P Harrison, F Dell'Isola, J Alsayednoor, and E Turco. Wrinkling in engineering fabrics: a comparison between two different comprehensive modelling approaches.

Proceedings of the Royal Society A: Mathematical, Physical and Engineering Sciences, 474(2216):20180063, 2018.

[Gio16] Ivan Giorgio. Numerical identification procedure between a micro-cauchy model and a macro-second gradient model for planar pantographic structures. *Zeitschrift für angewandte Mathematik und Physik*, 67(4):1–17, 2016.

[Gio20] Ivan Giorgio. A discrete formulation of kirchhoff rods in large-motion dynamics. *Mathematics and Mechanics of Solids*, 25(5):1081–1100, 2020.

[Gio21] Ivan Giorgio. Lattice shells composed of two families of curved kirchhoff rods: an archetypal example, topology optimization of a cycloidal metamaterial. *Continuum Mechanics and Thermodynamics*, 33(4):1063–1082, 2021.

[GR09] C. Geuzaine and J.-F. Remacle. Gmsh: A 3-d finite element mesh generator with built-in pre- and post-processing facilities. *International Journal for Numerical Methods in Engineering*, 79(11):1309–1331, 2009.

[Gre20] L Greco. An iso-parametric G^1-conforming finite element for the nonlinear analysis of kirchhoff rod. part i: the 2d case. *Continuum Mechanics and Thermodynamics*, 32(5):1473–1496, 2020.

[GRT17] Ivan Giorgio, Nicola Luigi Rizzi, and Emilio Turco. Continuum modelling of pantographic sheets for out-of-plane bifurcation and vibrational analysis. *Proceedings of the Royal Society A: Mathematical, Physical and Engineering Sciences*, 473(2207):20170636, 2017.

[Han00] P.C. Hansen. The L-Curve and its Use in the Numerical Treatment of Inverse Problems. In *in Computational Inverse Problems in Electrocardiology, ed. P. Johnston, Advances in Computational Bioengineering*, pages 119–142. WIT Press, 2000.

[HBC+16] F. Hild, A. Bouterf, L. Chamoin, F. Mathieu, J. Neggers, F. Pled, Z. Tomičević, and S. Roux. Toward 4D Mechanical Correlation. *Advanced Modeling and Simulation in Engineering Sciences*, 3(1):1–26, 2016.

[Koe84] Jan J Koenderink. What does the occluding contour tell us about solid shape? *Perception*, 13(3):321–330, 1984.

[Lak93] Roderic Lakes. Advances in negative poisson's ratio materials, 1993.

[Lam91] Horace Lamb. Xxiii. on the flexure of a flat elastic spring. *The London, Edinburgh, and Dublin Philosophical Magazine and Journal of Science*, 31(190):182–188, 1891.

[LNM+15] H. Leclerc, J. Neggers, F. Mathieu, F. Hild, and S. Roux. *Correli 3.0*. IDDN.FR.001.520008.000.S.P.2015.000.31500, Agence pour la Protection des Programmes, Paris (France), 2015.

[LVCF22] Gabriele La Valle, Alessandro Ciallella, and Giovanni Falsone. The effect of local random defects on the response of pantographic sheets. *Mathematics and Mechanics of Solids*, page 10812865221103482, 2022.

[MLG+18] Anil Misra, Tomasz Lekszycki, Ivan Giorgio, Gregor Ganzosch, Wolfgang H Müller, and Francesco Dell'Isola. Pantographic metamaterials show atypical poynting effect reversal. *Mechanics Research Communications*, 89:6–10, 2018.

[MW14] E. Maire and P. J. Withers. Quantitative X-ray tomography. *International Materials Reviews*, 59(1):1–43, 2014.

[PAG17] Luca Placidi, Ugo Andreaus, and Ivan Giorgio. Identification of two-dimensional pantographic structure via a linear d4 orthotropic second gradient elastic model. *Journal of Engineering Mathematics*, 103(1):1–21, 2017.

[Pre10] Andrew N Pressley. *Elementary differential geometry*. Springer Science & Business Media, 2010.

[PTM+22] Luca Placidi, Dmitry Timofeev, Valerii Maksimov, Emilio Barchiesi, Alessandro Ciallella, Anil Misra, and Francesco dell'Isola. Micro-mechano-morphology-informed continuum damage modeling with intrinsic 2nd gradient (pantographic) grain–grain interactions. *International Journal of Solids and Structures*, 254:111880, 2022.

[RHVB08] S. Roux, F. Hild, P. Viot, and D. Bernard. Three dimensional image correlation from X-Ray computed tomography of solid foam. *Composites Part A: Applied Science and Manufacturing*, 39(8):1253–1265, 2008.

[SAI11] Pierre Seppecher, Jean-Jacques Alibert, and Francesco Dell Isola. Linear elastic trusses leading to continua with exotic mechanical interactions. In *Journal of Physics: Conference Series*, volume 319, page 012018. IOP Publishing, 2011.

[SB21] Mario Spagnuolo and Emilio Barchiesi. Do we really need pantographic structures? In *Mathematical Applications in Continuum and Structural Mechanics*, pages 253–268. Springer, 2021.

[SdG+22] Maximilian Stilz, Francesco dell'Isola, Ivan Giorgio, Victor A Eremeyev, Georg Ganzenmüller, and Stefan Hiermaier. Continuum models for pantographic blocks with

second gradient energies which are incomplete. *Mechanics Research Communications*, page 103988, 2022.

[Sea08] George Frederick Charles Searle. *Experimental Elasticity: A Manual for the Laboratory*. University Press, 1908.

[Spa20] Mario Spagnuolo. Circuit analogies in the search for new metamaterials: Phenomenology of a mechanical diode. In *Altenbach H., Eremeyev V., Pavlov I., Porubov A. (eds) Nonlinear Wave Dynamics of Materials and Structures. Advanced Structured Materials, vol 122*, pages 411–422. Springer, Cham, Swizerland, 2020.

[Spa22] Mario Spagnuolo. Symmetrization of mechanical response in fibrous metamaterials through micro-shear deformability. *Symmetry*, 14(12):2660, 2022.

[SRCC22] Mario Spagnuolo, Emanuele Reccia, Alessandro Ciallella, and Antonio Cazzani. Matrix-embedded metamaterials: Applications for the architectural heritage. *Mathematics and Mechanics of Solids*, page 10812865221108372, 2022.

[SYP+22] Mario Spagnuolo, M Erden Yildizdag, Xavier Pinelli, Antonio Cazzani, and François Hild. Out-of-plane deformation reduction via inelastic hinges in fibrous metamaterials and simplified damage approach. *Mathematics and Mechanics of Solids*, 27(6):1011–1031, 2022.

[TC05] TCT Ting and Tungyang Chen. Poisson's ratio for anisotropic elastic materials can have no bounds. *The quarterly journal of mechanics and applied mathematics*, 58(1):73–82, 2005.

[TGCR16] Emilio Turco, Maciej Golaszewski, Antonio Cazzani, and Nicola Luigi Rizzi. Large deformations induced in planar pantographic sheets by loads applied on fibers: experimental validation of a discrete lagrangian model. *Mechanics Research Communications*, 76:51–56, 2016.

[TGGD17] Emilio Turco, Maciej Golaszewski, Ivan Giorgio, and Francesco D'Annibale. Pantographic lattices with non-orthogonal fibres: experiments and their numerical simulations. *Composites Part B: Engineering*, 118:1–14, 2017.

[TGMD17] Emilio Turco, Ivan Giorgio, Anil Misra, and Francesco Dell'Isola. King post truss as a motif for internal structure of (meta) material with controlled elastic properties. *Royal Society open science*, 4(10):171153, 2017.

[TMP+18] Emilio Turco, Anil Misra, Marek Pawlikowski, Francesco Dell'Isola, and François Hild. Enhanced piola–hencky discrete models for pantographic sheets with pivots without deformation energy: numerics and experiments. *International Journal of Solids and Structures*, 147:94–109, 2018.

[TTRMH14] T. Taillandier-Thomas, S. Roux, T.F. Morgeneyer, and F. Hild. Localized strain field measurement on laminography data with mechanical regularization. *Nuclear Instruments and Methods in Physics Research Section B*, 324:70–79, 2014.

[VVS+22] Malo Valmalle, Antoine Vintache, Benjamin Smaniotto, Florian Gutmann, Mario Spagnuolo, Alessandro Ciallella, and François Hild. Local-global dvc analyses confirm theoretical predictions for deformation and damage onset in torsion of pantographic metamaterial. *Mechanics of Materials*, page 104379, 2022.

[YBd20] M Erden Yildizdag, Emilio Barchiesi, and Francesco dell'Isola. Three-point bending test of pantographic blocks: numerical and experimental investigation. *Mathematics and Mechanics of Solids*, 25(10):1965–1978, 2020.

Appendices

A. DVC hardware and DVC parameters

Table 3 reports the hardware parameters of the experiment, and Table 4 the DVC parameters.

Table 3: DVC hardware parameters

Tomograph	North Star Imaging X50+
X-ray source	XRayWorX XWT-240-CT
Target / Anode	W (reflection mode)
Filter	none
Voltage	120 kV
Current	180 µA
Tube to detector	500 mm
Tube to object	272.685 mm
Detector	Dexela 2923
Definition	1536 × 1944 pixels (2 × 2 binning)
Number of projections	1200
Angular amplitude	360°
Frame average	5 per projection
Frame rate	10 fps
Acquisition duration	25 min 58 s
Reconstruction algorithm	filtered back-projection
Gray Levels amplitude	8 bits
Volume size	1723 × 491 × 813 voxels (after crop)
Field of view	143 × 40.75 × 67.48 mm^3 (after crop)
Image scale	83 µm/voxel

Table 4: DVC analysis parameters

DIC software	Correli 3.0 [LNM+15]
Image filtering	none
Element length (mean)	6 vx
Shape functions	linear (T4 elements [HBC+16])
Mesh	see Figure 4
Matching criterion	penalized sum of squared differences
Regularization length	$\ell_m = 25$ vx
Interpolant	cubic

B. Gray level residuals

The gray level residual fields are reported in Figure 17 for each loading step. The residual field was fairly homogeneous, except in the immediate vicinity of the supports (particularly at the top and bottom right), where high local flexure of the beam ends was not fully captured, partly because of the presence of cardboard. Higher RMS residuals found for the fourth scan were due to a residual field that had larger values on average throughout the sample. In that case, the larger deflection and especially more significant flexure of the beams produced a larger residual over the whole specimen.

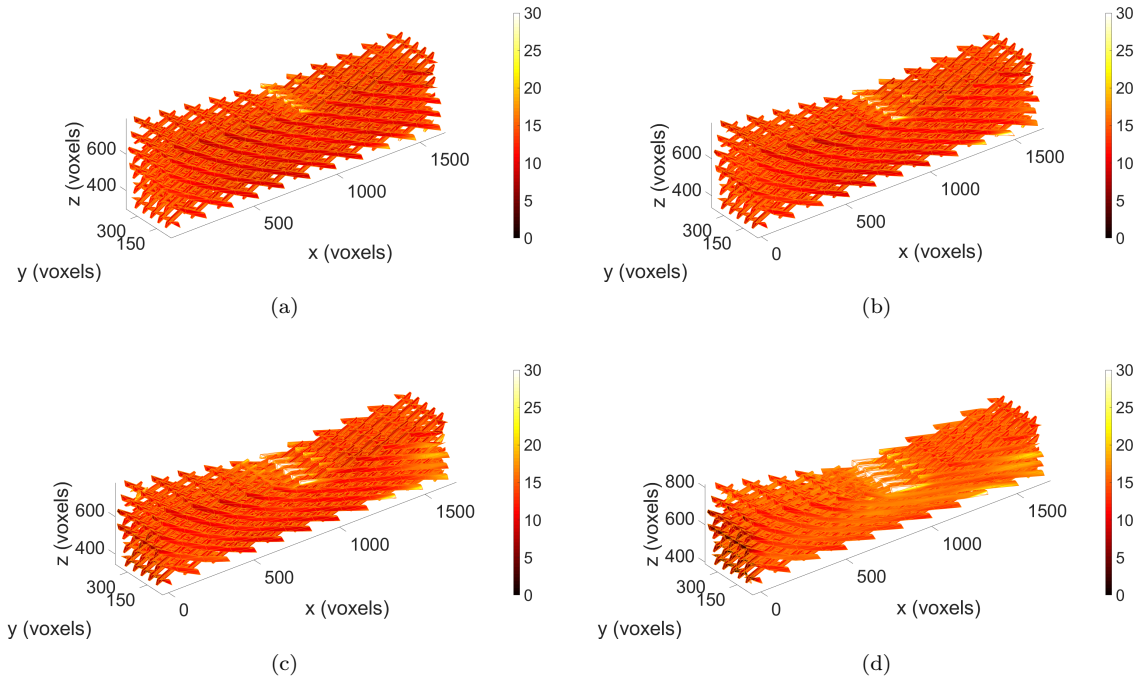

Figure 17: Gray level residual fields for the different considered loading steps: (a) 24 mm, (b) 29 mm, (c) 34 mm and (d) 39 mm deflections. Axis labels are expressed in voxels, the dynamic range for registered volumes was 255 (*i.e.,* 8 bits). The residuals are shown on the meshes in their deformed configuration.